CLUSTER CROSS SECTIONS FOR STRONG LENSING: ANALYTIC AND NUMERICAL LENS MODELS

MASSIMO MENEGHETTI[1,2], MATTHIAS BARTELMANN[2], LAURO MOSCARDINI[1]

[1]DIPARTIMENTO DI ASTRONOMIA, UNIVERSITÀ DI PADOVA, VICOLO DELL'OSSERVATORIO 2, I–35122 PADOVA, ITALY
[2]MAX-PLANCK-INSTITUT FÜR ASTROPHYSIK, P.O. BOX 1317, D–85748 GARCHING, GERMANY

ABSTRACT

The statistics of gravitationally lensed arcs was recognised earlier as a potentially powerful cosmological probe. However, while fully numerical models find orders of magnitude difference between the arc probabilities in different cosmological models, analytic models tend to find markedly different results. We introduce in this paper an analytic cluster lens model which improves upon existing analytic models in four ways. (1) We use the more realistic Navarro-Frenk-White profile instead of singular isothermal spheres, (2) we include the effect of cosmology on the compactness of the lenses, (3) we use elliptical instead of axially symmetric lenses, and (4) we take the intrinsic ellipticity of sources into account. While these improvements to the analytic model lead to a pronounced increase of the arc probability, comparisons with numerical models of the same virial mass demonstrate that the analytic models still fall short by a substantial margin of reproducing the results obtained with numerical models. **Using multipole expansions of cluster mass distributions, we show that the remaining discrepancy can be attributed to substructure inside clusters and tidal fields contributed by the cluster surroundings, effects that cannot reasonably and reliably be mimicked in analytic models.**

1. INTRODUCTION

Many authors pointed out that the statistics of gravitationally lensed arcs in galaxy clusters may be a powerful tool for constraining cosmological models. They are rare events caused by a highly nonlinear effect in cluster cores, and are thus not only sensitive to the cosmologically highly variable number density of galaxy clusters, but also to their internal structure.

The expected number of *giant* arcs, usually defined as arcs with a length-to-width ratio exceeding ten and apparent *B*-magnitude less than 22.5 [Wu & Hammer 1993], changes by orders of magnitude between low- and high-density universes according to the numerical models described in Bartelmann et al. (1998). They use the ray-tracing technique for studying gravitational lensing by galaxy cluster models taken from N-body simulations (see also Bartelmann & Weiss 1994; Bartelmann 1995; Bartelmann, Steinmetz & Weiss 1995; Meneghetti et al. 2000, 2001). This allows the most realistic description of the cluster lenses because all effects which could play an important role for the lensing phenomena are by construction taken into account. Cluster asymmetries, substructure, and the tidal field of the surrounding matter distribution are known to have substantial effects on arc statistics, and they are automatically included if the cluster simulations are suitably designed.

In order to extract useful cosmological constraints from arc statistics, it is essential to perform simulations on a fine grid in the cosmological parameter space. However, given the long computation times required for full numerical simulations of cluster lensing, it is currently not feasible to perform such simulations for sufficiently many combinations of the essential cosmological parameters, i.e. the matter density parameter Ω_0 and the cosmological constant Ω_Λ. Therefore, conclusions can so far be drawn only for discrete points in the Ω_0–Ω_Λ plane.

In a conceptually different approach, simple analytic, axially symmetric models have been used for describing the density profiles of cluster lenses (see e.g. Wu & Mao 1996; Cooray, Quashnock & Miller 1999; Molikawa et al. 1999; Kaufmann & Straumann 2000; Oguri, Taruya & Suto 2001; Oguri et al. 2002; Molikawa & Hattori 2001). This method of investigation has the advantage that the computation of the probability for arcs satisfying a specified property is fast and can easily be performed for a continuous and wide range of cosmological parameters, because the lensing properties of these models are perfectly known and fully described by analytic formulae. However, important effects like substructures or asymmetries in the matter distribution can at best be taken into account at an approximate level, and the correspondence between analytic and numerical models remains unclear. While the analytic studies by Cooray et al. (1999) and Kaufmann & Straumann (2000) find similar results as the numerical simulations regarding the sensitivity of arc statistics to the cosmic density parameter, their results are almost insensitive to the cosmological constant, in marked contrast to Bartelmann et al. (1998), who found order-of-magnitude changes in the arc cross sections between low-density models with and without a cosmological constant.

In this paper, we investigate whether the results of the analytic and numerical approaches can be reconciled using a more realistic analytic lens model. Previous analytic studies of arc statistics commonly used the singular isothermal sphere (hereafter SIS), which is computationally convenient, but has an unrealistic density profile and does not naturally reflect the theoretically expected and numerically demonstrated variations in halo concentration. Instead, we model cluster lenses as haloes with the density profile found by Navarro, Frenk & White (1997; hereafter NFW) in high-resolution simulations of haloes with a wide range of masses. The profile is flatter than isothermal near the core, and steeper outside, which leads to qualitatively and quantitatively different lensing properties. We take the change of halo concentration with halo mass and cosmology into account, we distort the lensing potential elliptically in order to mimic cluster asymmetries, and we adapt the ellipticity by fitting numerical cluster models. We then compare the efficiency for producing arcs with a minimal length-to-width ratio of the elliptical NFW lenses with fully numerically simulated cluster lenses, and with the singular isothermal spheres for reference.

The plan of the paper is as follows. In Sect. 2., we define the lensing cross section of both numerical and analytic models. In particular, in Sect. 2.1. we describe the ray-tracing simulations, and we show the lensing cross sections produced by a sample of five galaxy clusters simulated in three different cosmological

models. In Sect. 2.2., we deal with the lensing cross sections of axially symmetric analytic models and discuss the differences between SIS and NFW models. In Sect. 2.3., we show how the lensing cross sections change by assuming elliptical instead of circular sources. In Sect. 2.4., we discuss lensing by elliptically distorted NFW models and compare their arc cross sections with those of axially symmetric NFW lenses. In Sect. 3. we compare the analytic and the numerical models. Our conclusions are presented in Sect. 4..

2. CROSS SECTIONS FOR LONG AND THIN ARCS

The efficiency of a given lens for producing arcs with specified properties can be quantified by means of suitably defined lensing cross sections. They are defined as the areas on the source plane where sources must be located in order to be imaged as arcs satisfying the required conditions on, e.g., size, shape, magnitude and the like. We focus in this paper on the cross sections of clusters for producing long and thin arcs, i.e. for arcs whose length-to-width ratio L/W exceeds a given minimum value $(L/W)_{\mathrm{min}}$. In the following subsections, we describe our method for computing strong lensing cross sections of numerically and analytically modelled galaxy clusters.

2.1. Numerical models

For comparison to the analytic models, we compute the strong lensing cross sections of five numerically simulated cluster-sized dark-matter haloes, kindly made available by the GIF collaboration [Kauffmann et al. 1999]. The same clusters have been used by Bartelmann et al. (1998). They were obtained from N-body simulations performed in the framework of three different cosmological models. These are an Einstein-de Sitter model (hereafter SCDM); a flat, low-density universe with a matter density parameter $\Omega_0 = 0.3$ and a cosmological constant $\Omega_\Lambda = 0.7$ (ΛCDM); and an open, low-density model with $\Omega_0 = 0.3$ and $\Omega_\Lambda = 0$ (OCDM). The initial matter density in these models is perturbed about the mean according to a CDM power spectrum [Bond & Efstathiou 1984] with primordial spectral index $n = 1$, normalised such that the local abundance of massive galaxy clusters is reproduced (e.g. Viana & Liddle 1996). The complete list of cosmological parameters in these simulations is given in Bartelmann et al. (1998). The virial masses of the clusters at redshift $z = 0$ range between $\sim 5 \times 10^{14} M_\odot/h$ and $\sim 2 \times 10^{15} M_\odot/h$. The masses of individual particles are $1.0 \times 10^{10} h^{-1} M_\odot$ and $1.4 \times 10^{10} h^{-1} M_\odot$ for the high- and the low-Ω_0 models, respectively.

The lensing properties of these clusters are studied using a ray-shooting technique which was described in detail elsewhere (Bartelmann et al. 1998; Meneghetti et al. 2000, 2001). Here, we only briefly discuss some parameters used in these computations, and refer the reader to the cited papers for a more complete description.

Since strong lensing only occurs near the very cluster centres, we select areas of $1.5\,h^{-1}$ Mpc comoving side length centred on the lens centres. For all reasonable combinations of lens and source redshifts, this region is large enough to encompass the critical curves of the cluster lens, close to which large arcs form. A bundle of 2048×2048 rays is shot through a regular grid on the lens plane, covering the studied region, and their paths to the source plane are traced. We consider different snapshots of the cluster simulation at selected redshifts between $z_l = 0$ and $z_l = 1$. For each snapshot, three projections of each simulated cluster on orthogonal planes are used for performing the lensing simulations. The typical angular resolution at $z \approx 0.3$ is 0.18 arcsec, assuming the ΛCDM model.

The sources are assumed to all lie on one plane at redshift $z_s = 1$. Although real galaxy sources are obviously distributed in redshift, putting them all at the same redshift is acceptable because **first, observations show that most of the sources which experience strong lensing effects are generally at redshifts near unity** and second, the critical surface density changes very little with source redshift, unless it is very close to the lens redshift. Moreover, we assume sources to be elliptical, with their axis ratios b/a uniformly distributed in the range 0.5–1.0. An initial set of sources is placed on a regular grid covering the source plane, and additional sources are added on sub-grids whose resolution is iteratively increased towards the lens caustics. Thus, sources are placed on an adaptive hierarchy of grids in order to improve the numerical efficiency of the method and to increase the probability for finding long and thin arcs. For correcting the statistics of the numerically simulated arcs, we assign to each source and all of its images a statistical weight w which is inversely proportional to the squared resolution of the sub-grid on which the corresponding source was placed. The finer the grid resolution, the lower is the statistical weight of its images; see also Eq. (1) below.

Using the ray-tracing technique, we reconstruct the images of the background sources and measure their length, width and curvature radius. Our technique for image detection and classification was described in detail by Bartelmann & Weiss (1994) and adopted by Bartelmann et al. (1998) and Meneghetti et al. (2000, 2001). It results in a catalogue of simulated images which is subsequently analysed statistically.

Each source is taken to represent a fraction of the source plane. The cells of the sub-grid with the highest resolution have area A, and the sources placed on its grid points are given a statistical weight of unity. The absolute lensing cross sections for a specified image property are then determined by counting the statistical weights of the sources whose images have the required property. Specifically, we search for sources with a length-to-width ratio exceeding a threshold $(L/W)_{\mathrm{min}}$. If a source has multiple images with $(L/W) \geq (L/W)_{\mathrm{min}}$, we multiply its statistical weight by the number of such images. Therefore, the lensing cross section is

$$\sigma_{(L/W)_{\mathrm{min}}} = A \sum_i W_i w_i n_i \, , \qquad (1)$$

where W_i is unity if the i-th source has images with $(L/W) \geq (L/W)_{\mathrm{min}}$ and zero otherwise, n_i is the number of images of the i-th source satisfying the required condition, and w_i is the statistical weight of the source.

2.2. Axially symmetric models

For sufficiently simple, axially symmetric lens models, the strong lensing cross sections can be also computed in an analytic or semi-analytic way. We consider two such models, the singular isothermal sphere (SIS) for reference, and haloes with the NFW density profile [Navarro et al. 1997]. The SIS has been very widely used in many previous studies on arc statistics because of its computational simplicity. The NFW density profile fits the results of highly resolved numerical halo simulations and thus provides a much more realistic description of cluster density profiles than the SIS profile. We focus on the NFW profile here, but give some results for SIS lenses for later comparison.

The SIS density profile is given by

$$\rho(r) = \frac{\sigma_v^2}{(2\pi G r^2)} \, , \qquad (2)$$

where σ_v is the velocity dispersion. The NFW density profile is

$$\rho(r) = \frac{\rho_s}{(r/r_s)(1 + r/r_s)^2} \, , \qquad (3)$$

where ρ_s and r_s are characteristic density and distance scales, respectively (see Navarro et al. 1997). These two parameters are not independent, but related to a single parameter, which can be taken as the cluster mass. It is important to note that ρ_s and r_s also depend on the cosmological model, hence the lensing properties of haloes with identical mass are different in different cosmological models, a crucial property which the simpler singular isothermal sphere models do not share. **For instance, the halo concentration, which is the ratio between the virial and the scale radius, changes from ~ 4.4 to ~ 6.2 for a halo of mass $5 \times 10^{14} h^{-1} M_\odot$ at redshift** 0.3 **in low-density cosmological models with $\Omega_0 = 0.3$ if the cosmological constant is changed from $\Omega_\Lambda = 0.7$ to zero.** The NFW halo falls off more steeply than isothermal at radii beyond r_s, but flattens towards the halo centre. These different features lead to markedly different lensing properties of the NFW compared to the SIS model, as will be shown below (see also the discussion in Perrotta et al. 2002).

For axially symmetric lens models, the lens equation is essentially one-dimensional. Define the optical axis as the line running from the observer through the lens centre, and introduce physical distances from the optical axis ξ and η, respectively, on the lens and source planes. Fixing a length scale ξ_0 on the lens plane, we can define the dimensionless distance $x \equiv \xi/\xi_0$. The chosen length scale ξ_0 is projected onto the length scale $\eta_0 = \xi_0 D_s/D_l$ on the source plane, where D_l and D_s are the angular-diameter distances to the lens and source planes, respectively. In analogy to the lens plane, a dimensionless distance from the optical axis $y \equiv \eta/\eta_0$ can now be defined on the source plane. The lens equation, relating the position of an image on the lens plane to that of its source on the source plane is then

$$y = x - \alpha(x) \, , \qquad (4)$$

where $\alpha(x)$ is the reduced deflection angle at distance x from the lens centre, caused by the lensing mass distribution. It is the gradient of the lensing potential ψ,

$$\alpha(x) = \frac{d\psi(x)}{dx} \, . \qquad (5)$$

See, e.g. Schneider, Ehlers & Falco (1992) and Narayan & Bartelmann (1997) for more details.

Local imaging properties are described by the Jacobian matrix of the lens mapping. It has two eigenvalues, λ_r and λ_t, which describe the image distortion in the radial and the tangential directions, respectively. For an axially symmetric lens, they are

$$\lambda_r(x) = 1 - \frac{d\alpha}{dx} \, , \quad \lambda_t(x) = 1 - \frac{\alpha}{x} \, . \qquad (6)$$

Analytic expressions for the lensing potential $\psi(x)$ at any distance x are easily obtained for the SIS and the NFW lens models. Therefore, the eigenvalues of the Jacobian matrix can straightforwardly be computed for both lens models considered here.

For a SIS lens, the lensing potential is

$$\psi(x) = |x| \, , \qquad (7)$$

if $\xi_0 = 4\pi(\sigma_v/c)^2 D_l D_{ls}/D_s$ is chosen as a length scale, where D_{ls} is the angular diameter distance between lens and source. Hence, the deflection angle and the eigenvalues are

$$\alpha(x) = \frac{x}{|x|} \, , \quad \lambda_r = 1 \, , \quad \lambda_t = 1 - \frac{1}{|x|} \, . \qquad (8)$$

For an NFW lens, we take $\xi_0 = r_s$ for simplicity and define $\kappa_s \equiv \rho_s r_s \Sigma_{cr}^{-1}$, where $\Sigma_{cr} = [c^2/(4\pi G)] [D_s/(D_l D_{ls})]$ is the critical surface mass density for strong lensing. We then have the lensing potential

$$\psi(x) = 4\kappa_s \left[\frac{1}{2} \ln^2 \frac{x}{2} - 2\,\mathrm{arctanh}^2 \sqrt{\frac{1-x}{1+x}} \right] \, , \qquad (9)$$

which implies the deflection angle

$$\alpha(x) = \frac{4\kappa_s}{x} \left[\ln \frac{x}{2} + \frac{2}{\sqrt{1-x^2}} \mathrm{arctanh} \sqrt{\frac{1-x}{1+x}} \right] \, , \qquad (10)$$

from which the eigenvalues $\lambda_{r,t}$ can straightforwardly be derived. Several different aspects of lensing by haloes with NFW or generalised NFW profiles can be found in Bartelmann (1996), Wright & Brainerd (2000), Li & Ostriker (2002), Wyithe, Turner & Spergel (2001), Perrotta et al. (2002). It can easily be verified that the potential [Eq. (9)] satisfies the Poisson equation $\nabla^2 \psi = 2\kappa$, with κ given in Bartelmann (1996).

It is an important feature of the NFW lensing potential [Eq. (9)] that **its radial profile** is considerably less curved near the centre than the SIS potential [Eq. (7)]. Since the local imaging properties are determined by the curvature of ψ, this immediately implies substantial changes to the lensing properties. At fixed halo mass, the critical curves of an NFW lens are closer to its centre than for a SIS lens because of its flatter density profile. There, the potential is less curved, thus the image magnification is larger and decreases more slowly away from the critical curves. Therefore, NFW lenses are less efficient in image splitting than SIS lenses, but comparably efficient in image magnification. What is more important here is that any additional shear added to a flat lensing potential (e.g. by asymmetries) much more strongly extends the critical curves than for a steeper potential. We will see the consequences below.

The inverse of the eigenvalues $\lambda_{r,t}$ of the Jacobian matrix gives the radial and the tangential magnifications at the radial distance x from the lens centre. The points satisfying the conditions $\lambda_{r,t} = 0$ form the radial or tangential critical curves, respectively, where the corresponding magnifications tend to infinity. For SIS lenses, λ_r is always unity, hence the radial critical curve does not exist in this case, so the images are not radially magnified. The tangential critical curve is the circle $|x| = 1$. For NFW lenses, the critical curves have to be found numerically. In the limit of small κ_s, when the critical curves are close to the lens centre, we find to first order in x

$$\lambda_t \approx 2 \exp \left(-\frac{1 + \kappa_s}{2\kappa_s} \right) \, , \quad \lambda_r \approx \frac{\lambda_t}{2.718} \, . \qquad (11)$$

By means of the lens equation, the critical curves are mapped to the corresponding caustic curves in the source plane. For the axially symmetric lenses we are considering, the tangential caustic degenerates to the point where the optical axis intercepts the source plane.

2.3. Elliptical sources

The length-to-width ratio of an image depends on the local lens properties and on the ellipticity of the sources. We derive and compare results for both circular and elliptical sources. Since the source galaxies are typically much smaller than the length scale on which the lens properties change substantially, we can assume that the length-to-width ratio of the images of a circular source is given by the ratio of the two eigenvalues $q_l \equiv \lambda_r/\lambda_t$ at the image position.

An elegant model for introducing elliptical sources into analytic lensing calculations was recently proposed by Keeton (2001). Following his approach, the observed length-to-width ratio L/W is a function of three variables, which are the intrinsic axis ratio $q_s = a/b$ and the intrinsic position angle θ of the source, and the eigenvalue ratio q_l of the lens at the image position:

$$L/W = \left[\frac{T + (T^2 - 4Q)^{1/2}}{T - (T^2 - 4Q)^{1/2}}\right]^{1/2} , \qquad (12)$$

where

$$T = q_l^2 + q_s^2 + (q_l^2 - 1)(q_s^2 - 1)\cos^2\theta , \qquad (13)$$
$$Q = q_l^2 q_s^2 . \qquad (14)$$

The length-to-width ratio L/W of each image can be related to the source position y by means of the lens equation. For sources with fixed intrinsic shape and orientation lensed by axially symmetric lenses, L/W monotonically decreases as the source is moved from $y = 0$ (where the degenerate tangential caustic is located) away from the lens centre. Thus the lensing cross section for arcs with $L/W \geq (L/W)_{\min}$ from sources with intrinsic axis ratio q_s and position angle θ can be written as

$$\sigma_{(L/W)_{\min}}(q_s, \theta) = \pi y_{\min}^2 , \qquad (15)$$

where $y_{\min}$ is the distance from the optical axis where L/W falls below $(L/W)_{\min}$.
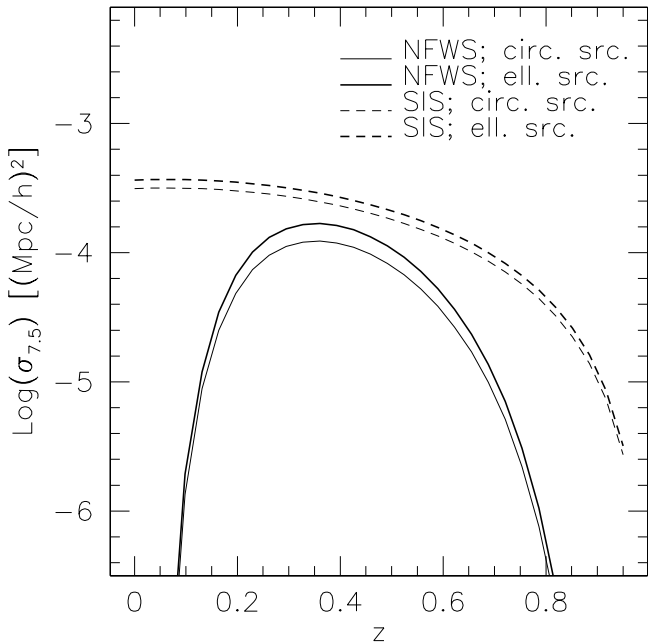

FIG. 1.—Cross sections $\sigma_{7.5}$ for the formation of arcs with length-to-width ratio larger than 7.5 as functions of lens redshift. Results are shown for a virial lens mass of $M = 10^{15} h^{-1} M_\odot$ in a ΛCDM cosmology. Two different lens models are used: the axially symmetric NFW lens model (solid curves), and the singular isothermal sphere for comparison (dashed lines). Thick and thin curves were obtained assuming intrinsically circular and elliptical sources, respectively.

In order to compute the final lensing cross section, we have to average these cross sections over all the possible values of q_s and θ. For doing so, we assume that θ and q_s^{-1} are uniformly distributed in the ranges $[0, \pi]$ and $[0.5, 1]$, respectively. This agrees with the assumptions underlying the numerical simulations. Therefore, the final lensing cross section is given by

$$\sigma_{(L/W)_{\min}} = \frac{4}{\pi} \int_1^2 \int_0^{\pi/2} \sigma_{(L/W)_{\min}}(q_s, \theta) \, d\theta \frac{dq_s}{q_s^2} . \qquad (16)$$

Both SIS and NFW lenses can produce multiple images for suitable source positions. For SIS lenses, multiple images occur only for sources lying inside the Einstein ring, which has the angular radius $\theta_E = (4\pi\sigma_v^2/c^2)(D_{ls}/D_s)$. If this is the case, the lens produces an arc and a counter-arc. As the source moves towards the Einstein ring, the tangential magnification of the counter-arc decreases and tends to zero. Then, the counter-arc disappears (see Narayan & Bartelmann 1997 for further detail). The main "arc" remains, but its tangential magnification goes to unity as the source moves away from the optical axis towards infinity.

For NFW lenses, multiple images occur only for sources with $y < y_{c,r}$, where $y_{c,r}$ is the radius of the radial caustic. As shown by Bartelmann (1996), the NFW density profile always has a radial critical curve (and thus a radial caustic) for any combination of ρ_s and r_s. Sources inside the radial caustic therefore always produce a radial image, an arc, and a counter-arc. We neglect the radial image because it is radially oriented. As for SIS lenses, the arc and the counter-arc have different length-to-width ratios L/W. In fact, the counter-arc is radially magnified as the source moves towards the radial caustic, and its length-to-width ratio decreases more rapidly than that of the main tangential arc. Therefore, two separate cross sections must be computed for both SIS and NFW lens models, one for the arc and one for the counter-arc, and the total lensing cross section is the sum of these two contributions.

To give an example, Fig. 1 shows the lensing cross section for arcs with length-to-width ratio $L/W > 7.5$ produced from sources at redshift $z_s = 1$ by a lens with mass $10^{15} h^{-1} M_\odot$ at redshifts between zero and unity. Results are given for the ΛCDM model. The solid lines correspond to NFW lenses, the dashed lines to SIS lenses. Thick and thin lines indicate the results for elliptical and circular sources, respectively.

As expected, the lensing cross section of the NFW model is smaller than for SIS lenses because of its flatter density profile. In particular, NFW lenses lose their strong-lensing efficiency when the lens approaches the observer or the sources. Conversely, due to its unrealistically steep and scale-free density profile, the SIS remains an efficient strong lens even when it is located very close to the observer or to the source.

The relative increase of the cross section for the intrinsically elliptical sources is virtually independent of the lens redshift, but it does depend on the lens model. In fact, the relative change in the lensing cross sections for NFW lenses is approximately twice as high as for SIS lenses, quite independent of the lens redshift. This is again due to the shallower lensing potential of NFW compared to SIS lenses.

2.4. Elliptical models

The construction of lens models with elliptical or pseudo-elliptical isodensity contours is generally quite complicated (see e.g. Kassiola & Kovner 1993; Kormann, Schneider & Bartelmann 1994; Golse & Kneib 2002). Starting from an elliptical lensing potential is computationally much more tractable, but has the disadvantage that the mass distribution corresponding to the elliptical potential can become dumbbell-shaped even for moderate ellipticities, which is unwanted for galaxy lenses. Galaxy clusters, however, are less relaxed and exhibit substructure, so for them dumbbell-shaped mass distributions are uncritical. For this reason, we prefer constructing elliptical cluster
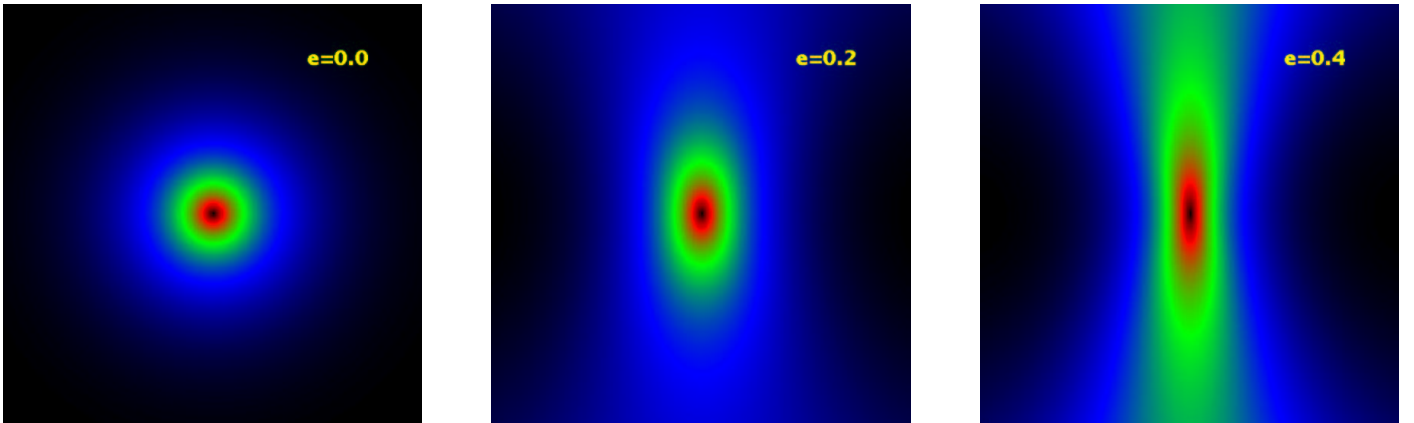
FIG. 2.—Deflection-angle maps for the axially symmetric (left panel) and the elliptically distorted NFW lens model, for ellipticities $e = 0.2$ (central panel) and $e = 0.4$ (right panel). The side length of each panel is $\sim 6'$. See the text for more detail.

lens models starting directly from the effective lensing potential. Moreover, since the NFW density profile gives a much more realistic reproduction of the simulated clusters than the SIS, we chose to generalise only the NFW lens model to the elliptical case.

The lensing potential of an axially symmetric NFW lens was given in Eq. (9) above. We introduce the ellipticity $e \equiv 1 - b/a$, where a and b are the major and minor axes of the ellipse, by substituting

$$x \to X = \sqrt{\frac{x_1^2}{(1-e)} + x_2^2(1-e)}, \qquad (17)$$

where x_1 and x_2 are the two Cartesian components of x, $x^2 = x_1^2 + x_2^2$. This ensures that the mass inside circles of fixed radius remains constant as the ellipticity changes.

The Cartesian components of the deflection angle are then

$$
\begin{aligned}
\alpha_1 &= \frac{\partial \psi}{\partial x_1} = \frac{x_1}{(1-e)X} \hat{\alpha}(X), \\
\alpha_2 &= \frac{\partial \psi}{\partial x_2} = \frac{x_2(1-e)}{X} \hat{\alpha}(X),
\end{aligned}
\qquad (18)
$$

where $\hat{\alpha}(X)$ is the unperturbed (i.e. axially-symmetric) deflection angle at the distance X from the lens centre.

Using these formulae, deflection-angle fields for different values of the ellipticity e are readily computed. Some examples for deflection-angle maps are displayed in Fig. 2. Obviously, the shape of the contours becomes more and more elliptical as e is increased. We analyse the lensing properties of these deflection-angle fields using the ray-tracing technique and, finally, compute the lensing cross sections, adopting the same techniques as applied to the numerical models.

Increasing the ellipticity of the lensing potential strengthens the shear field of the lens, and consequently the tangential caustic expands and changes. Examples for the change of the caustics with ellipticity e are shown in Fig. 3, which refers to a halo with mass $M = 10^{15} h^{-1} M_\odot$ at redshift $z = 0.3$, and the underlying cosmology is the ΛCDM model. As discussed above, the radial and tangential caustics are a circle and a point, respectively, for the axially symmetric models. Increasing e, the caustics stretch, develop cusps, and enclose a growing area. Thus the lensing cross sections are expected to grow rapidly. This is confirmed by Fig. 4, which shows cross sections for arcs with $L/W \geq 7.5$. These results were obtained through ray-tracing

simulations in which deflection angle maps for two haloes of mass $M = 7.5 \times 10^{14} h^{-1} M_\odot$ and $M = 10^{15} h^{-1} M_\odot$ were used. Again, we adopt the ΛCDM model universe and put the lens at redshift $z = 0.3$. Increasing the ellipticity of the lensing potential from $e = 0$ to $e = 0.5$, the cross section increases approximately by a factor of 30, almost independently of the lens mass considered.

3. COMPARISON OF ANALYTIC AND NUMERICAL MODELS

We can now compare the strong lensing cross sections of the numerical and analytic models introduced in the preceding sections. For that purpose, we focus on the lensing cross sections for the formation of arcs with length-to-width ratios L/W larger than 7.5 and 10. As described before, we compare them to the lensing properties of five numerical models of galaxy cluster haloes, picking simulation snapshots at twelve different redshifts between zero and unity. For clarity, we present here the results obtained for the most massive halo only. The behaviour of the cross sections for the other numerical models is in good qualitative and quantitative agreement with that obtained for this cluster.

The results are illustrated in Fig. 5, where the dotted lines refer to the fully numerically simulated cluster, while solid and dashed lines represent the cross sections of NFW and SIS lenses, respectively, having the same virial mass as the numerical cluster model. Finally, the shaded regions in the same plots show the cross sections obtained by elliptically distorting the NFW lensing potential with ellipticities e in the range between $e = 0.2$ and $e = 0.4$ (lower and upper limits, respectively). Results are shown for $L/W = 7.5$ (upper panels) and $L/W = 10$ (lower panels), and they were obtained for the SCDM (left panels), ΛCDM (central panels), and OCDM models (bottom panel).

First, we checked the calibration of the analytic relative to the numerical cross sections. For doing so, we performed ray-tracing simulations using the axially symmetric deflection angle maps for the NFW lens model, and used them for determining the strong-lensing cross sections. The results are shown as filled dots in the panels of Fig. 5. The very good agreement with the analytic estimates obtained as explained in Sect. 2.2. demonstrates the reliability of our numerical technique.

The general trends in the lensing cross sections shown in Fig. 5 can be understood as follows. The strong-lensing efficiency of a mass distribution depends on several factors. First, for the light coming from the sources to be focused on the observer, the lens must be located at a suitable distance from both
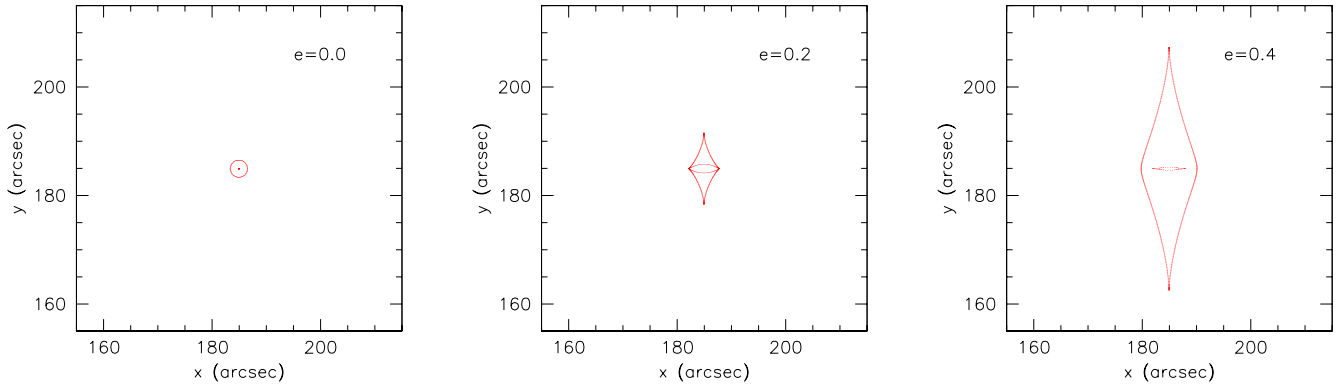
FIG. 3.—Caustic curves produced by an NFW halo with mass $M = 10^{15}\,h^{-1}\,M_\odot$ at redshift $z = 0.3$ in a ΛCDM universe. Different panels show results for different ellipticities e of the lensing potential: $e = 0$, i.e. axially symmetric (left panel); $e = 0.2$ (central panel) and $e = 0.4$ (right panel). The figure demonstrates that even small or moderate elliptical distortions substantially stretch the caustic curves, and thus cause the arc cross sections to grow considerably.
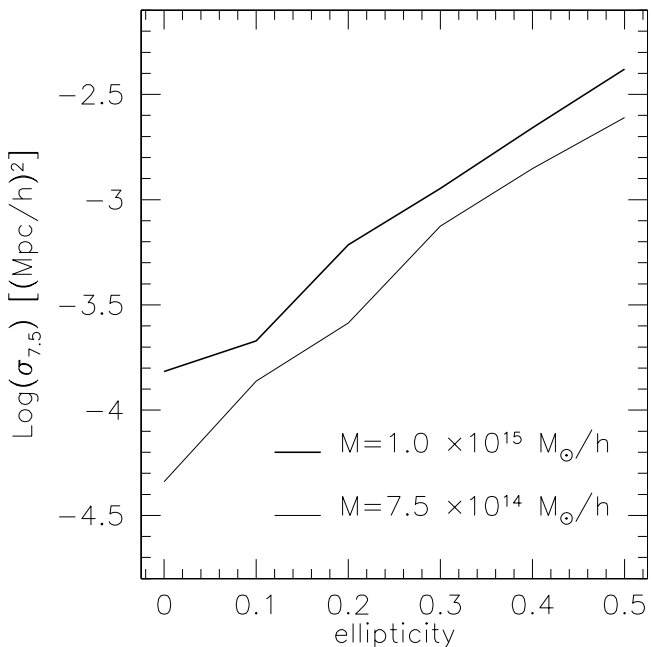

FIG. 4.—Strong-lensing cross section $\sigma_{7.5}$ of elliptically distorted NFW lenses for arcs with length-to-width ratio larger than 7.5 as a function of the ellipticity e of the lensing potential. Tick and thin lines were calculated for haloes of mass $M = 10^{15}\,h^{-1}\,M_\odot$ and $M = 7.5 \times 10^{14}\,h^{-1}\,M_\odot$, respectively, both placed at $z = 0.3$ in a ΛCDM cosmology.

the observer and the sources. Second, the larger the (virial) mass of the lens is, the stronger are the lensing effects it produces close to its centre. Finally, the more concentrated the lens is, the thinner are the long arcs expected to be.

Since the lens mass grows with decreasing redshift because new material is accreted by the halo and deepens its potential well, the lensing cross sections are expected to grow as well. On the other hand, when the lens is too close to the observer, the cross section is geometrically suppressed, unless the lens surface density profile is sufficiently steep and scale-free, as for the SIS lenses. In fact, in this case the focusing by the lens is strong enough to allow observers to see strongly distorted images of

background sources also in very near lenses, i.e. at relatively small redshifts (see also Fig. 1).

Moreover, the results are expected to depend on cosmology. In fact, in the OCDM and ΛCDM models, galaxy clusters become efficient lenses at higher redshift than in the SCDM scenario, because they form earlier and are centrally more concentrated. This is confirmed by our numerical results. In the Einstein-de Sitter case both $\sigma_{7.5}$ and σ_{10} are completely negligible for redshifts $z \gtrsim 0.4$–0.5 and peak at $z \approx 0.2$, while for low-density models the cross sections are largest in the redshift range $0.3 \lesssim z \lesssim 0.5$. A more complete discussion on the dependence of lensing cross sections on cosmology can be found in Bartelmann et al. (1998).

In this paper, we concentrate on comparing the cross sections of the analytic and numerical models. As Fig. 5 shows, the numerical models generally have much larger cross sections than the analytic models. In particular, the cross sections for axially symmetric NFW lenses are almost two orders of magnitude smaller, quite independent of the cosmological models considered. For SIS lenses, the discrepancy with the numerical models is only partially compensated by the unrealistically steep central density profile, but the estimated values of $\sigma_{7.5}$ and σ_{10} remain too low. Introducing the elliptical distortion into the NFW lens model allows the cross section to increase by roughly an order of magnitude compared to the axially symmetric NFW model, but even then the analytic cross sections fail to reproduce the numerical cross sections unless unrealistically high values of e are adopted.

Fig. 5 also demonstrates that apart from the cross-section amplitude, the analytic models miss another important feature of the numerical results, which show steep increases and decreases reflecting merger events. While a merging sublump approaches a cluster, the cross section tends to increase because of the increasing tidal field, and as the cluster relaxes following the merger event, the cross section decreases again. It becomes quite clear from Fig. 5 that such events play an important role in understanding realistic cluster cross sections, and they cannot reasonably be captured in analytic models unless their prime advantage of being computationally fast is sacrificed.

3.1. Ellipticity estimates

It is important to check which ellipticities are typical for the lensing potential of the numerical clusters. To this end, we compare the deflection-angle maps constructed for the numer-
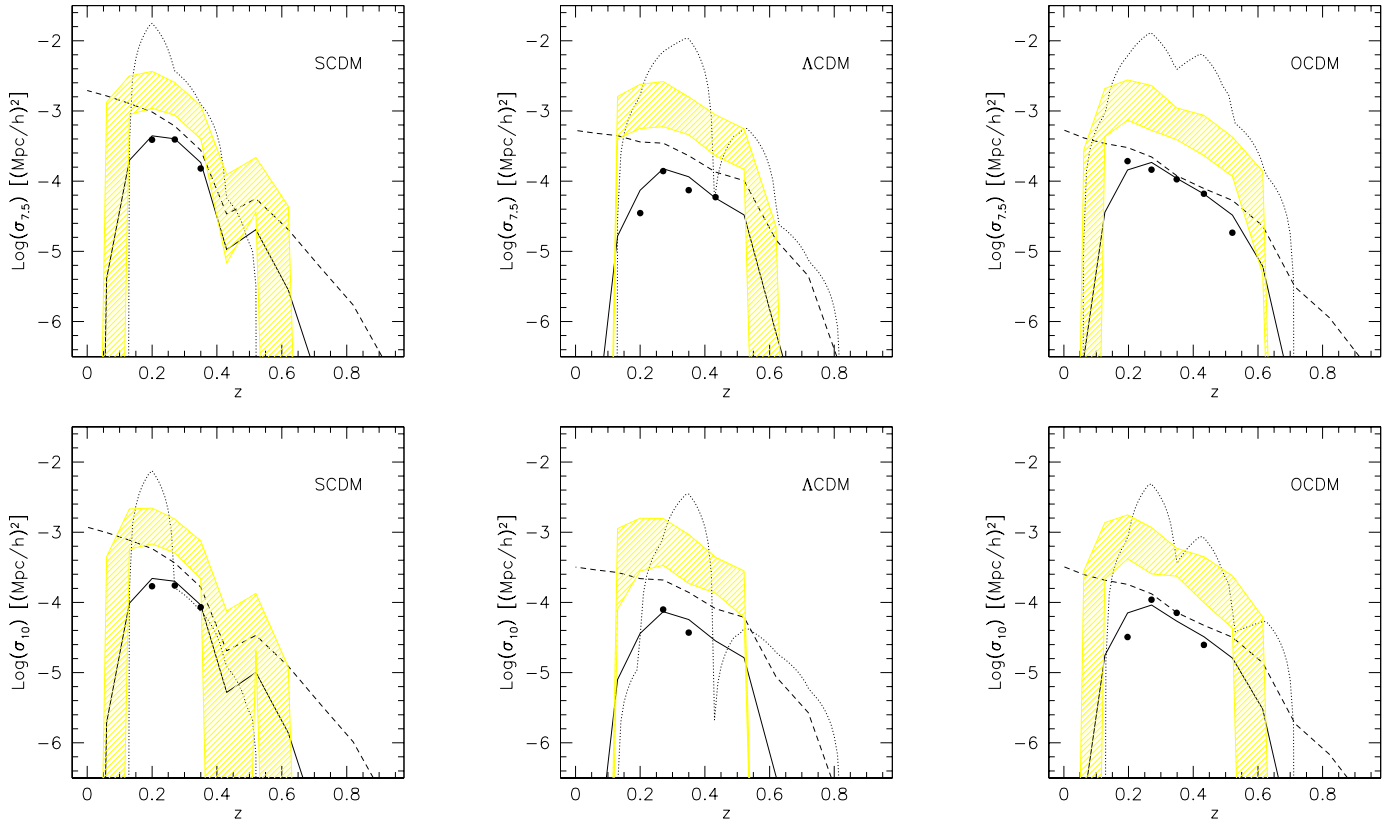
FIG. 5.—Lensing cross sections for arcs with length-to-width ratio larger than 7.5 ($\sigma_{7.5}$; top panels) and 10 (σ_{10}; bottom panels) as a function of the lens redshift. Results for different cosmologies are shown: SCDM (left panels), ΛCDM (central panels) and OCDM (right panels). Dotted lines show results obtained from the analysis of the most massive halo in the numerically simulated sample; solid and dashed lines represent the cross sections predicted by the axially symmetric NFW and SIS models, respectively, with the same virial mass as the numerically modelled halo. The shaded regions mark the cross sections obtained with the elliptically distorted NFW lens model, with ellipticities ranging between $e = 0.2$ and $e = 0.4$ (lower and upper limits, respectively). The filled dots are the lensing cross sections found by ray-tracing simulations with the deflection angle maps of the axially symmetric NFW lens model. Their agreement with the analytic curves demonstrates the reliability of our numerical method.

ical haloes with those obtained for elliptical NFW lenses with identical virial mass. We estimate the best-fit ellipticity e by minimising the mean-square deviation

$$\chi^2 = \sum_i \left(\frac{\alpha_i - \hat{\alpha}_i}{\hat{\alpha}_i} \right)^2 , \qquad (19)$$

where α_i and $\hat{\alpha}_i$ are the deflection angles of the light ray passing through the i-th grid point on the numerical and the elliptical lens model, respectively. The summation is done over all grid points contained in the central region of roughly $\sim 200 \, h^{-1} \, \text{kpc}$ comoving side length. This way, we measure the ellipticity of the lensing potential in the central region close to the critical curves which is the most relevant for our purposes. For this test, we use the simulation snapshots at $z = 0.27$, which is approximately the redshift where the numerical haloes reach their maximum lensing efficiency. The complete sample of five numerical clusters and three independent projections per cluster was used for this analysis.

The results are reported in Tab. 1. Median ellipticities of $e \sim 0.3$ are found, with only a weak dependence on cosmology. Indeed, only little evolution of the ellipticity is found going from low to high-density cosmological models. The median ellipticities in the OCDM and the ΛCDM models are slightly smaller than in the SCDM case, as expected, given that clusters form earlier in these models and have more time to relax.

Anyway, as the semi-interquartile ranges (SIQR) show, the ellipticity distributions are quite broad, in particular for SCDM. The same analysis has also been repeated using other simulation snapshots, corresponding to redshifts in the range $0.2 \lesssim z \lesssim 0.7$. The results are quite similar to the previous ones and therefore not given in the table. The typical median of e is around 0.3, and exceeds 0.4 in only a few cases. In conclusion, the ellipticities measured in the lensing potential of the numerical clusters are insufficient for reconciling the cross sections of elliptically distorted NFW models with the fully numerical results.

3.2. Substructure estimates

The remaining difference between numerical and analytical cross sections must be attributed to some factors which are missing from the analytical models. The most important of those is certainly the presence of substructure in the lensing mass distribution.

Deviations of the projected mass distribution of a numerically simulated cluster from the predictions of circular or elliptical models can be quantified by means of a multipole expansion of its surface density field. For performing this analysis, we first define a reference frame whose origin coincides with the surface density peak of the cluster. Then, starting from the particle positions in the N-body simulations, we compute the surface density at discrete radii r_n and
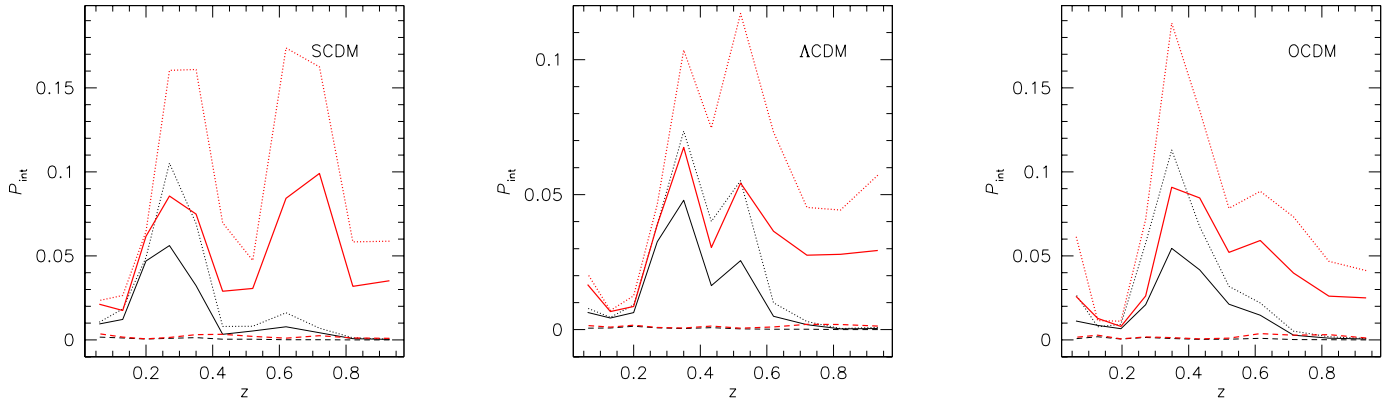
FIG. 6.—Integrated multipole power as a function of redshift for the most massive cluster in our numerically simulated sample. Results for three different cosmologies are shown; SCDM (left panel), ΛCDM (central panel) and OCDM (right panel). Heavy dotted and dashed lines show the results of multipole expansions of the cluster surface mass density at cluster-centric distances of $r_1 = 1.25\,h^{-1}$Mpc and $r_0 = 155\,h^{-1}$kpc, respectively, and heavy solid lines show the area-weighted averages of the integrated power within r_1 (see text for more details). Light lines show the results of rescaling the heavy curves with the cluster virial masses and the effective lensing distance.

TABLE 1.—Ellipticities e of the lensing potential obtained by fitting the deflection-angle maps of the elliptically distorted NFW lens model to fully numerical deflection angles. We give the medians (second column) and semi-interquartiles ranges (SIQR; third column) for the ellipticities found in our cluster sample for different cosmological models (indicated in the first column). Results are shown for the simulation snapshots at redshift $z = 0.27$.

cosmological model	median	SIQR
SCDM	0.320	0.102
ΛCDM	0.305	0.032
OCDM	0.270	0.052

position angles ϕ_k, with r_n and ϕ_k taken from the intervals $[0, 1.5]\,h^{-1}$Mpc and $[0, 2\pi]$, respectively. For any given r_n, each discrete sample of data $\Sigma(r_n, \phi_k)$ can be expanded into a Fourier series in the position angle,

$$\Sigma(r_n, \phi_k) = \sum_{l=0}^{\infty} S_l(r_n) e^{-il\phi_k} , \qquad (20)$$

where the coefficients $S_l(r_n)$ are given by

$$S_l(r_n) = \sum_{k=0}^{\infty} \Sigma(r_n, \phi_k) e^{il\phi_k} , \qquad (21)$$

and can be computed using fast-Fourier techniques. We define the power spectrum $P_n(l)$ of the multipole expansion l as $P_n(l) = |S_l(r_n)|^2$.

Axially symmetric and elliptical models have very simple multipole expansions. For a circular mass distribution, only the monopole, $l = 0$, contributes to the sum in Eq. (20). An elliptical mass distribution has one more contribution from the quadrupole, $l = 2$. The dipole term, $l = 1$, is zero for both these models. Of course, the surface density fields of numerically simulated clusters are much more complex than those of our analytic models. Their multipole expansions contain a dipole and also multipoles of higher order than two, which correspond to substructures spanning opening angles of order $\sim \pi/l$ when seen from the cluster centre.

Therefore, in order to quantify the amount of substructure and the degree of asymmetry in the mass distributions of our numerically simulated lenses at any distance r_n from the cluster centre, we can use the power spectra $P_n(l)$. In particular, we define an integrated power $P_{\rm int}(r_n)$, which is the sum of the power spectral densities of the dipole and of all multipoles of higher order than two, i.e. we subtract the monopole and quadrupole contributions from the total integrated power,

$$P_{\rm int}(r_n) = \sum_{l=0}^{\infty} P_n(l) - P_n(0) - P_n(2) . \qquad (22)$$

This quantity measures the deviation from an elliptical distribution of the surface mass density at a given distance r_n from the cluster centre. In order to suppress the dependency on the radial coordinate, we also compute the area-weighted averaged value of $P_{\rm int}$ inside radius r as

$$\bar{P}_{\rm int}(r) = \frac{2}{r^2} \sum_{r_n \leq r} P_{\rm int}(r_n)\, r_n \Delta r_n . \qquad (23)$$

In Fig. 6, we show how the integrated power $\bar{P}_{\rm int}(r)$ changes as a function of the cluster redshift for those lenses whose cross sections were plotted in Fig. 5. Again, we show the results for all three cosmological models. For making the integrated power at different radii comparable, we normalise them to the power of the corresponding monopole. Moreover, we average the results obtained for the three projections of the same cluster. The heavy dotted and dashed lines show the results for radii $r_1 = 1.25\,h^{-1}$Mpc, comparable to the cluster virial radius, and $r_0 = 155\,h^{-1}$kpc. For comparison, the heavy solid curves indicate the area-weighted power inside circles of radius r_1 as a function of redshift. The small values reached by the heavy dashed curves indicate that in the very central region of the cluster the mass distribution is dominated by the monopole and the quadrupole terms, i.e. in the innermost regions of the clusters, the surface mass density has elliptical iso-contours. Moreover, these curves are flat, which means that the surface density contours remain elliptical at all redshifts between zero and unity. On the other hand, as shown by the heavy dotted and solid lines, at distances comparable to the virial radius or smaller the

contribution to the power from the dipole and the multipoles of higher order than two is large and can even exceed 15% of the monopole contribution.

A quick comparison of these curves to the lensing cross sections in Fig. 5 shows that the redshifts where the contributions of the dipole and the higher-order multipoles are largest correspond quite well to those where the numerical cross sections deviate most strongly from those of the elliptical models.

This is most obvious between redshifts 0.2 and 0.4, where also the geometrical lensing efficiency is largest. At lower and higher redshifts, the lensing cross sections drop for two major reasons; first, the lenses are too close to the observer or to the sources; second, the cluster virial mass decreases with increasing redshift. For better comparing the dependences on redshift of the integrated power and the lensing cross sections, we rescale $\bar{P}_{int}$ with the effective lensing distance, $D = D_l D_{ds}/D_s$ and with the virial cluster mass. The thin lines in Fig. 6 show $\bar{P}_{int}$ after rescaling. The damping effect almost completely removes the peaks in the integrated power at redshifts higher than $z \sim 0.5 - 0.6$, as well as those at redshifts lower than $z \sim 0.2$, and make the curves much more similar to the curves displaying the lensing cross sections as a function of redshift in Fig.5.

This correlation between the higher-order multipoles of the mass distributions and the cross sections proves that substructures and asymmetries are the dominant reason for the discrepancy between numerical and analytical lensing cross sections. We verified that the peaks in the integrated power $\bar{P}_{int}$ occur when clumps of matter enter within the virial radius of the respective clusters. Then, the lensing cross section grows for two reasons; first, because the cluster mass increases, and second, because of the increased shear produced by the substructures falling towards the cluster centres.

4.   SUMMARY AND DISCUSSION

In this paper, we have investigated an analytic lens model with NFW density profile and elliptically distorted lensing potential for its ability to reproduce the statistics of strong-lensing events in galaxy clusters. It improves upon previously used models in four ways. First, the commonly adopted singular isothermal density profile is replaced by the NFW profile, which is much more adequate for cluster-sized haloes. Second, this model allows the effect of cosmology on the lens concentration to be included. Third, we elliptically perturb the model for approximating the substantial effect of cluster asymmetries on their strong-lensing cross sections. Fourth, we take into account that sources are intrinsically elliptical rather than circular. We adapt the ellipticity of this lens model to fit numerically simulated clusters and compare the strong-lensing cross sections of the analytic model to those of fully numerically simulated clusters. Results for singular isothermal sphere lenses are given for comparison. Our results can be summarised as follows:

- The cross section of the axially symmetric NFW lens model for arcs with length-to-width ratio larger than 7.5 and 10 are almost two orders of magnitude smaller than those of simulated clusters.

- The axially symmetric singular isothermal lens model is more efficient for strong lensing because its density profile is steeper in the core, but its large-arc cross sections are still smaller than the numerical ones by typically an order of magnitude, except at low redshift where both the numerical

models and the NFW model fail in producing any lensing effect.

- The comparatively flat lensing potential of haloes with the NFW density profile makes NFW lenses poor image splitters, but efficient magnifiers. In addition, the flat potential renders the lensing properties very sensitive to changes in the tidal field, because small deformations of the potential can lead to large shifts of the critical curves.

- The cross sections of our new elliptical model increase steeply and monotonically as a function of ellipticity. An ellipticity of ≈ 0.3 typically increases the cross sections by an order of magnitude. However, for the model to reproduce the arc cross sections of the numerical clusters, unrealistically high ellipticities $e \gtrsim 0.5$ are required.

- Comparing the deflection angle maps to those of elliptical NFW lens models with variable e, we estimated the ellipticity of the lensing potential in the central region of the numerically modelled haloes and found typical ellipticities of $e \sim 0.3$, substantially below values required to solve the discrepancy between analytic and numerical lens models.

- The change of the fully numerical cluster cross sections with time exhibits pronounced signatures of merger events. As merging sublumps approach the cluster centre, their tidal field markedly increases the strong-lensing cross section. **We have verified this by means of a multipole expansion of the cluster surface density field, which shows that larger deviations of the lensing cross section of the numerical clusters from the prediction of the analytic models arise when the contribution to the surface density power spectra from the dipole and from higher-order multipoles is large.** Our comparison of elliptical analytic lens models with fully numerical models shows that an adequate description of such events is necessary for an accurate calculation of arc cross sections.

We conclude that even our improved analytic model is unable to reproduce the strong lensing properties of realistic cluster models, which we assume the fully numerically simulated haloes to be. We have seen that the axially symmetric NFW lens model underpredicts the number of arcs with length-to-width ratio exceeding a given threshold by approximately two orders of magnitude compared to the fully numerical results.

At present, the NFW density profile can be considered the most realistic model profile for cluster haloes (see, however, Moore et al. 1999; Jing & Suto 2000). Moreover, it allows to take the effect of varying halo concentration on the strong lensing efficiency into account, which is a substantial advantage compared to the commonly used SIS density profile. Finally, the profile permits analytical calculations of the relevant lensing properties. Therefore, the NFW density profile appears ideally suited for constructing analytic models for strong lensing by clusters, in particular if elliptical distortions are included, as we have done in our extension of the model.

However, the differences remaining between the fully numerical and analytic approaches indicate that analytic modelling is still insufficient for properly and accurately describing strong lensing by galaxy clusters. We showed that the most important missing factors are the presence of substructures within the clusters, and the tidal field of the surrounding matter distribution. In fact, significant substructure is abundant in and around numerically simulated haloes. They enhance the shear field around the clusters, increasing the length of the critical curves and consequently increase the probability of forming long arcs.

Of course, the elliptically distorted NFW lens model is adequate for good qualitative calculations of arc probability, as Fig. 5 shows. **Detailed cluster mass models have demonstrated that lensing in individual clusters can be reproduced at an impressively accurate level (e.g. Kneib et al. 1993). However, for deriving precise constraints on cosmology or the structure and evolution of the cluster population as a whole, full numerical simulations of many clusters seem to be the only reliable choice.**

REFERENCES

Bartelmann M., 1995, A&A, 299, 11
Bartelmann M., 1996, A&A, 313, 697
Bartelmann M., Huss A., Colberg J.M., Jenkins A., Pearce F.R., 1998, A&A, 330, 1
Bartelmann M., Steinmetz M., Weiss A., 1995, A&A, 297, 1
Bartelmann M., Weiss A., 1994, A&A, 298, 1
Bond J.R., Efstathiou G., 1984, ApJ, 285, L45
Cooray A.R., Quashnock J.M., Miller M.C., 1999, ApJ, 513, 95
Golse G., Kneib J.-P., 2002, A&A, 387, 788
Jing Y.P., Suto Y., 2000, ApJ, 529, 69
Kassiola A., Kovner I., 1993, ApJ, 417, 450
Kauffmann G.A.M., Colberg J.M., Diaferio A., White S.D.M., 1999, MNRAS, 303, 188
Kaufmann R., Straumann N., 2000, Ann. Phys., 11, 507
Keeton C.R., 2001, ApJ, 562, 160
Kneib J. P., Mellier Y., Fort B., Mathez, G., 1993, A&A, 273, 367
Kormann R., Schneider P., Bartelmann M., 1994, A&A, 284, 285
Li L.-X., Ostriker J.P., 2002, ApJ, 566, 652
Meneghetti M., Bolzonella M., Bartelmann M., Moscardini L., Tormen G., 2000, MNRAS, 314, 338
Meneghetti M., Yoshida N., Bartelmann M., Moscardini L., Springel V., Tormen G., White S.D.M., 2001, MNRAS, 325, 435
Molikawa K., Hattori M., 2001, ApJ, 559, 544
Molikawa K., Hattori M., Kneib J.-P., Yamashita K., 1999, A&A, 351, 413
Moore B., Quinn T., Governato F., Stadel J., Lake G., 1999, MNRAS, 310, 1147
Narayan R., Bartelmann M., 1997, in Dekel A., Ostriker J.P., eds, Formation of Structure in the Universe. Cambridge Univ. Press, Cambridge, p. 360
Navarro J.F., Frenk C.S., White S.D.M., 1997, ApJ, 490, 493
Oguri M., Taraya A., Suto Y., 2001, ApJ, 559, 572
Oguri M., Taraya A., Suto Y., Turner E.L., 2002, ApJ, 568, 488
Perrotta F., Baccigalupi C., Bartelmann M., de Zotti G., Granato G.L., 2002, MNRAS, 329, 445
Schneider P., Ehlers E.E., Falco E., 1992, Gravitational Lenses. Springer Verlag, Berlin
Viana, P.T.P., Liddle, A.R., 1996, MNRAS, 281, 323
Wright C.O., Brainerd T.G., 2000, ApJ, 534, 34
Wu X.P., Hammer F., 1993, MNRAS, 262, 187
Wu, X.-P., Mao, S., 1996, ApJ, 463, 404
Wyithe J.S.B., Turner E.L., Spergel D.N., 2001, ApJ, 555, 504